Ring-exchange interaction effects on magnons in the Dirac magnet $CoTiO_3$

Yufei Li,[1] Thuc T. Mai,[2] M. Karaki,[1] E. V. Jasper,[1] K. F. Garrity,[3] C. Lyon,[1] D. Shaw,[4] T. DeLazzer,[4] A. J. Biacchi,[5] R. L. Dally,[6] D. M. Heligman,[1] J. Gdanski,[1] T. Adel,[2] M. F. Muñoz,[2] A. Giovannone,[1] A. Pawbake,[7] C. Faugeras,[7] J. R. Simpson,[8,2] K. Ross,[4] N. Trivedi,[1] Y. M. Lu,[1] A. R. Hight Walker,[2] and R Valdés Aguilar[1,*]

[1]*Department of Physics, The Ohio State University. Columbus, Ohio 43210, USA*
[2]*Quantum Measurement Division, Physical Measurement Laboratory, NIST, Gaithersburg, Maryland 20899, USA*
[3]*Materials Measurement Science Division, Materials Measurement Laboratory, NIST, Gaithersburg, Maryland 20899, USA*
[4]*Department of Physics, Colorado State University, Fort Collins, Colorado 80523, USA*
[5]*Nanoscale Device Characterization Division, Physical Measurement Laboratory, NIST, Gaithersburg, Maryland 20899, USA*
[6]*NIST Center for Neutron Research, National Institute of Standards and Technology, Gaithersburg, Maryland 20899, USA*
[7]*Laboratoire National des Champs Magnetiques Intenses, LNCMI-EMFL, Grenoble, France*
[8]*Department of Physics, Astronomy, and Geosciences, Towson University, Towson, Maryland 21252, USA*

(Received 23 February 2024; accepted 29 April 2024; published 21 May 2024)

The magnetic interactions that determine magnetic order and magnon energies typically involve only two spins. While rare, multispin interactions can also appear in quantum magnets and be the driving force in the ground-state selection and in the nature of its excitations. By performing time-domain terahertz and magneto-Raman spectroscopy measurements combined with theoretical modeling, we determine the origin of the magnon excitation gap in Dirac antiferromagnet $CoTiO_3$. By adding a ring-exchange interaction in a hexagonal plaquette of the honeycomb lattice to both an XXZ spin model and to a low-energy spin-orbital flavor wave model, a gap is generated in the magnon spectrum at the Brillouin zone center. With this addition, the flavor wave model reproduces a large swath of experimental results including terahertz, Raman, inelastic neutron scattering, and magnetization experiments.

DOI: 10.1103/PhysRevB.109.184436

I. INTRODUCTION

In magnetically ordered materials with localized electrons, the fundamental magnetic interactions result from the exchange of electrons [1–3]. Typically, only the interaction between pairs of electrons' spins is considered to explain the nature of the ground state and its excitations, whereas three-, four-, and six-spin interactions are ignored. When these higher-order interactions occur in a loop they are called cyclic or ring exchange. Such interactions have only been documented in a few cases: bulk and thin films of solid ^{3}He [4–8], in the high-T_c parent compound La_2CuO_4 [9,10], more recently in a honeycomb cobaltite [11], and in a kagome magnet [12].

Here, we provide an additional instance of the importance of ring exchange on a quantum material. We use a combination of time-domain terahertz (THz) spectroscopy (TDTS) and magneto-Raman spectroscopy to measure the temperature and magnetic field dependence of the low energy magnetic excitations in $CoTiO_3$. In this proposed Dirac topological magnon material [13,14], the origin of the energy gap in the magnon spectrum at the Brillouin zone center has remained undetermined until now. Our study provides a detailed examination of the two lowest-energy magnons. We deduce that the gap opens due to the ring-exchange interaction between the six Co^{2+} spins on a hexagon. This interaction also explains the selection rules of the THz magnon absorption and their magnetic field dependence. Finally, we clarify that topological surface magnons are not expected in $CoTiO_3$. Our results highlight the importance of the small, but finite, many-spin interactions on the magnetic ground state and its excitations.

The classification of topological materials has brought about a new perspective on the properties of solid-state systems [15,16]. This has been used to discover new electronic topological states of matter and has increased the possibilities for producing material properties by design [17,18]. More recently, the pursuit of materials where the interplay between topology and magnetism generates topological magnon excitations has begun [19]. $CoTiO_3$, for example, is proposed to have a topological Dirac crossing between its magnon bands. While new materials have been predicted to host topologically protected magnons on their surfaces [20,21], their conclusive experimental demonstration remains an open problem. Here we address whether $CoTiO_3$ can host such topologically protected surface magnons.

$CoTiO_3$ has a layered structure with space group $R\bar{3}$. The Co atoms form a buckled honeycomb lattice in the hexagonal plane, where each atom is either slightly above or below a plane. These ferromagnetic planes are stacked antiferromagnetically along the c [001] axis [14,22], see Fig. 1(a), so-called type-A antiferromagnetism. An antiferromagnetic phase transition occurs at the Néel temperature of

*valdesaguilar.1@osu.edu

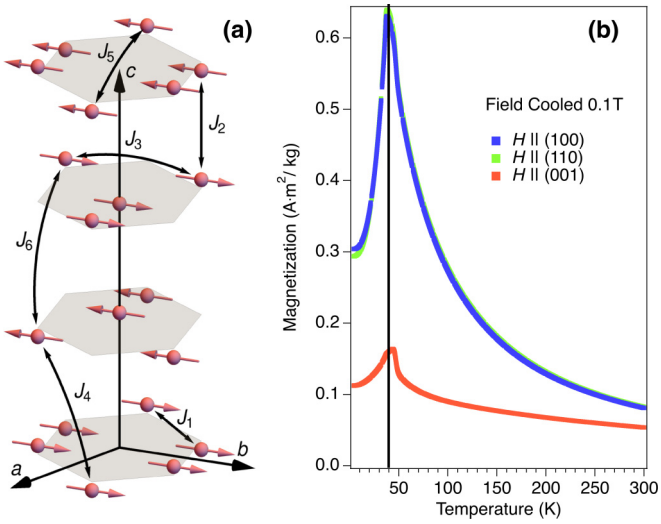

FIG. 1. Magnetic structure and magnetization in $CoTiO_3$. (a) Magnetic structure of $CoTiO_3$ as determined by elastic neutron scattering with lattice constants $a = b = 5.064$ Å and $c = 13.91$ Å [13,14,27]. Parallel Co spins reside on the vertices of buckled honeycomb planes stacked antiferromagnetically along the c axis. Magnetic pair interactions J_1 through J_6 are indicated. (b) Magnetization parallel (blue and green lines) and perpendicular (red line) to the honeycomb plane of the single crystals used for the TDTS and Raman measurements. The Néel temperature is indicated by the black vertical line.

$T_N = 38(3)$ K [23–26]. In this phase, the Co spins are ferromagnetically aligned within the honeycomb plane but, due to the lattice symmetry, the spin direction cannot be uniquely determined [14,27]. This direction is typically described to be along the b axis [010].

The magnetic degrees of freedom for Co^{2+} ions in a trigonally distorted octahedral environment are composed of spin and orbital angular momenta where $S = 3/2$ and the effective $l = 1$, respectively [28]. Taking into account spin-orbit coupling and the distorted octahedral environment, the local atomic electronic states form six doublets where the lowest-energy state can be considered to have an effective spin of $\tilde{S} = 1/2$ [13,29,30]. The interactions between neighboring Co^{2+} have been calculated in this octahedral environment [29–31]. When projected into the $\tilde{S} = 1/2$ space, these interactions generate Heisenberg, Kitaev, and off-diagonal symmetric exchange couplings. The theoretical phase diagram for a two-dimensional honeycomb lattice of Co^{2+} atoms includes a Kitaev quantum spin liquid [32], vortex, zigzag, and ferromagnetic phases [31]. $CoTiO_3$ is in the latter phase where these ferromagnetic planes stack antiferromagnetically.

This $\tilde{S} = 1/2$ approximation in the XXZ Hamiltonian captures many of the features seen by inelastic neutron scattering in $CoTiO_3$ [13,14]. However, it is insufficient to explain the details of the low-energy magnetic scattering spectra. In an XXZ Hamiltonian, the spin components in the honeycomb plane interact with different strength than the z components. These experiments also found that first spin-orbital excited state has finite dispersion in momentum space and that its energy is only twice as large as the bandwidth of the low-energy excitations [14,33]. In addition, the magnon spectrum of the effective $\tilde{S} = 1/2$ spins in the XXZ Hamiltonian is gapless at the zone center, while experiments indicate that there is a gap of approximately 1 meV [13,14]. These observations imply that the effective $\tilde{S} = 1/2$ picture of the XXZ Hamiltonian within linear spin wave theory is not sufficient to fully describe the magnetic excitations in $CoTiO_3$. While a quantum order-by-disorder mechanism [34] was proposed in Ref. [14] to explain the opening of the gap in $CoTiO_3$, its magnitude is too small compared to the experimentally estimated one. Below, we resolve these issues with the combination of a detailed TDTS and magneto-Raman spectroscopy study of the low-energy magnetic dynamics in single crystals of $CoTiO_3$ as a function of temperature and magnetic fields, accompanied by an expanded theoretical model.

II. RESULTS

Figure 1(b) shows the magnetization of the single crystals on which TDTS and Raman experiments were performed (details of the crystal growth and magnetization measurements are given in Ref. [35]). A clear antiferromagnetic phase transition is detected at 38 K, identified by a vertical line in the figure. No temperature hysteresis was observed, indicating a continuous phase transition, as found earlier [24–26].

In TDTS transmission measurements, magnon absorption is identified by the decrease of the transmission in a narrow frequency range centered at the magnon frequency below the magnetic ordering transition temperature [36,37] (details of TDTS are given in Ref. [35]). We describe below the magnon absorptions observed in $CoTiO_3$ and show them in Fig. 2. Figures 2(a)–2(c) show three different polarization configurations of the THz electric ($\boldsymbol{e}_\omega$) and magnetic ($\boldsymbol{h}_\omega$) fields for three different crystal cuts. Figures 2(a) and 2(c) show that, when $\boldsymbol{h}_\omega$ is parallel to the honeycomb plane, one main absorption mode dominates the spectra below T_N with an energy of approximately 5.4 meV (≈1.3 THz) at 8 K. This energy coincides with one of the magnon modes at the zone center reported previously [13,14], which thus confirms this magnetic dipole absorption as a magnon. The shallow minimum around 1 meV in Fig. 2(a) is present for all temperatures shown even above T_N, and thus it cannot be ascribed to a magnon absorption.

The inset in Fig. 2(b) shows an additional low-energy absorption that also coincides with a magnon observed in neutron spectroscopy, though we determine its energy to be ≈0.9 meV (≈0.23 THz). This is slightly lower than estimated in Ref. [14] and different from a previous antiferromagnetic resonance measurement on a powder sample [38]. This mode is referred to as a pseudo-Goldstone mode and corresponds to the small oscillatory deviations of the magnetic moment in the honeycomb plane. These deviations cost no energy when there is no in-plane anisotropy. The selection rules for this mode cannot be completely determined because it could only be observed weakly for the combination of $\boldsymbol{h}_\omega \parallel [001]$ and $\boldsymbol{e}_\omega \parallel$ to the honeycomb plane [Fig. 2(b)]. If the mode is purely magnetic dipole, then it should be observable only in this configuration.

Raman scattering experiments show the same two magnons observed with TDTS at zero magnetic field but, due to the narrower peaks in the Raman experiment, the energies of these magnons are determined more precisely: 0.82(5) and

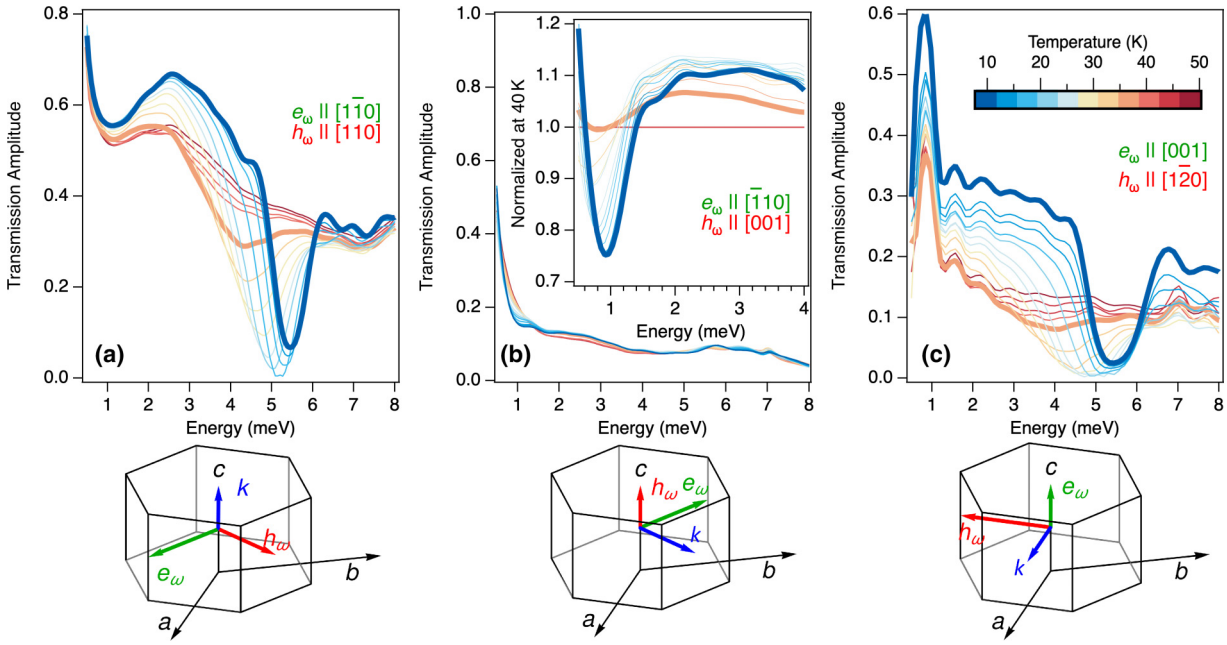

FIG. 2. THz magnon spectrum of $CoTiO_3$. Each of the three panels is composed of the THz transmission spectrum on top and on the bottom is the polarization configuration drawn with respect to the non-Bravais hexagonal lattice indicating the direction of the THz electric ($\boldsymbol{e}_\omega$) and magnetic ($\boldsymbol{h}_\omega$) fields and their propagation direction ($\boldsymbol{k}$). (a) Transmission spectrum for $\boldsymbol{e}_\omega$ and $\boldsymbol{h}_\omega$ both in the honeycomb plane showing one prominent absorption mode at ≈5.4 meV and ≈1.3 THz. (b) Spectrum with $\boldsymbol{h}_\omega$ perpendicular to the honeycomb plane and $\boldsymbol{e}_\omega$ parallel to it with no strong features present. The inset shows the transmission spectra normalized to the 40-K spectrum. An absorption mode at ≈ 0.9 meV and ≈ 0.23 THz is active below T_N. (c) Transmission spectra with $\boldsymbol{h}_\omega$ parallel to the honeycomb plane and $\boldsymbol{e}_\omega$ perpendicular to it. These show the same mode identified in panel (a). The data in panels (a) and (c) show that the 5.4-meV magnon is only active when $\boldsymbol{h}_\omega$ is parallel to the honeycomb plane, making it a magnetic dipole mode. Because the 0.9 meV mode is only observed in the panel (b) configuration, we cannot determine if it is active for other directions of $\boldsymbol{e}_\omega$ and $\boldsymbol{h}_\omega$.

5.37(5) meV, details are given in Ref. [35]. Figure 3(a) shows the results of the magneto-Raman scattering experiment for magnetic fields smaller than 9 T with orthogonal (crossed) polarization configuration, with $\boldsymbol{e}_{\text{in}}$ and $\boldsymbol{e}_{\text{out}}$ denoting incident and scattered linear polarizations. The measurement was carried out on a crystal cut perpendicular to the c axis, the same crystal whose THz data are shown in Fig. 2(a). The external static magnetic field is applied parallel to the a-b plane. In addition to the magnons at low energy, several modes at higher energy become active below T_N. These correspond to the spin-orbital excitations reported before [14,33] and to additional phonons that become active at the zone center because of the doubling of the unit cell size with magnetic order. The detailed investigation of these modes, including their response to applied magnetic fields will be reported elsewhere [39].

In a magnetic field applied parallel to the honeycomb plane, the Raman spectra show that the energies of the two lowest magnon modes shift significantly, as shown in Fig. 3(a). For larger magnetic fields up to 22 T in the hexagonal plane, a separate experiment was performed in the high-magnetic-field laboratory (LNCMI) in Grenoble, France, with unpolarized light at a sample temperature of 5 K. Figure 3(b) shows the results of fitting the low-energy Raman peaks both at low- and high-magnetic fields with Gaussian functions to obtain the magnetic field dependence of their energies (circle markers), along with model fitting results (lines) that are discussed in the next section. The magnon energies seem to cross around ≈11 T indicating little to no coupling between these magnons. As the field increases, their energies separate further until one magnon reaches the lowest measurable energies around ≈17 T. The signal of this magnon is completely absent above this field, marking a phase transition to the fully polarized state. A magnetic field up to 7 T applied along the c axis does not shift the magnons in any measurable way as shown in Ref. [35].

III. DISCUSSION

The data presented above reveal a zone-center magnon gap of ≈0.9 meV at 8 K, as measured by TDTS [Fig. 2(b)] and 0.82(5) meV by Raman spectroscopy [Fig. 3(a)]. A second, higher-energy magnon is observed as an in-plane magnetic dipole THz absorption [Figs. 2(a) and 2(c)] and is also detected in the Raman data [Fig. 3(a)]. The magnetic field dependence of these two magnons was also obtained for both in-plane and out-of-plane static magnetic fields.

Our data confirm the existence of a magnon gap that previous theoretical models fail to adequately capture. We address this inadequacy by expanding on two models proposed in Ref. [14]. The first model treats the magnetic moments as only coming from the lowest spin-orbital doublet of the Co^{2+} ion (described above), the effective $\tilde{S} = 1/2$ model (in Ref. [35]). The second model, the flavor wave model, takes into account all six spin-orbital doublets and expresses them by bosonic operators [40], which are described in Ref. [35]. We add to

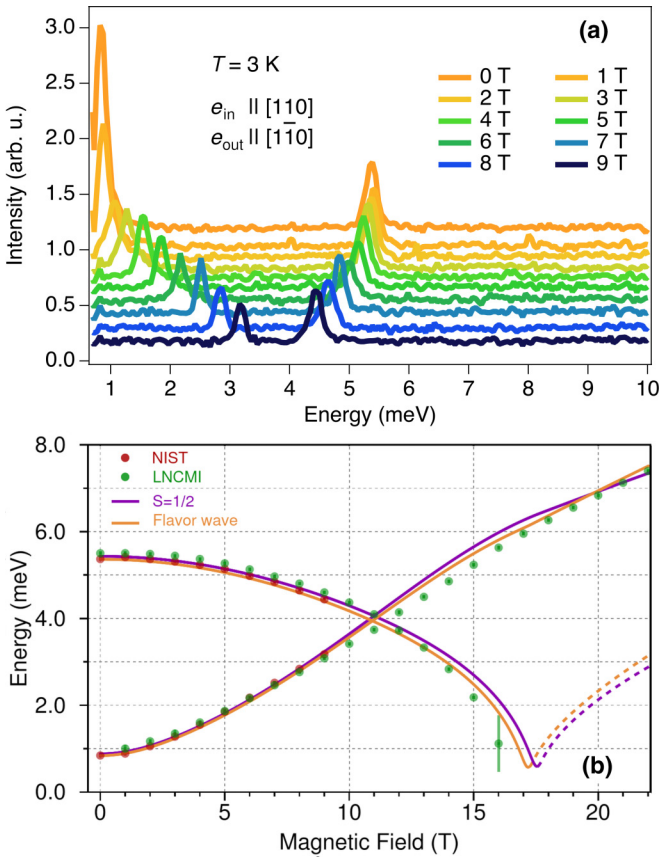

FIG. 3. Magnetic field dependence of Raman spectra. (a) Raman spectra at 3 K of the two lowest-energy magnons for fields up to 9 T applied parallel to the honeycomb plane. (b) Fit of the field dependence of the magnon energies using both the $\tilde{S} = 1/2$ model (purple) and the flavor wave model (orange). The dashed lines above ∼17 T indicate that this mode has finite momentum and is unobservable with Raman scattering.

these model Hamiltonians (details in Table I) a gap opening ring-exchange interaction that functions as an effective six-fold anisotropy for the magnetic moments in the honeycomb plane. This generates a term in the free energy proportional to $\cos(6\phi)$, where ϕ is the angle between the spin direction and the a axis.

The form of the ring-exchange interaction we use is $r(e^{-i\phi_6}\sum_{\boldsymbol{r}}\prod_{i=1}^{6} S^{+}_{\boldsymbol{r}+\boldsymbol{\delta}_i^{\text{ring}}} + \text{H.c.})$, where r is either $\tilde{\alpha}_6$ or α_6 for the effective $\tilde{S} = 1/2$ or the flavor wave models, respectively. ϕ_6 is an angle that determines the direction of the spins within the honeycomb plane in the ground state. This represents the simultaneous exchange of six spins within a hexagon of the honeycomb plane as schematically shown in Fig. 4(a). The ring-exchange interaction strength $\alpha_6 \approx 0.62$ μeV within the flavor wave model and of $\tilde{\alpha}_6 \approx 46$ μeV in the $\tilde{S} = 1/2$ approximation can open a gap consistent with the TDTS, Raman, and neutron experiments. It is a remarkable result that such small values of the ring exchange can open such a sizable gap of ≈0.9 meV, even though they are more than 2 orders of magnitude smaller than the gap itself and the nearest-neighbor exchange interaction J_1. A simple estimate of the expected value of the ring exchange $\tilde{\alpha}_6$ is $6!J_1^3/U^2$, where J_1 is the nearest-neighbor exchange interaction, U is the on-site Hubbard interaction, and the factorial term is a combinatorial factor that counts how many of these ring-exchange terms contribute to the Hamiltonian. Using the value $U \approx 3.25$ eV from Ref. [41] and the nearest neighbor J_1 from the effective $\tilde{S} \approx 1/2$ model, we obtain $\tilde{\alpha}_6 \approx 17$ μeV, which is of the same order of magnitude as obtained from our fit. In the flavor wave model, we also added a biquadratic exchange between nearest neighbors with strength q. While this term does not open a gap, we add it to better fit the higher-energy (>24 meV) excitations observed in the Raman experiments [39] and in Refs. [14,33].

The magnetic field dependence of the magnon energies [Fig. 3(b)] is also reproduced by these two models. In the $\tilde{S} = 1/2$ model we require an effective in-plane g factor of $\tilde{g}_{||} = 2.73(3)$ in addition to the XXZ Hamiltonian with the 12 exchange parameters on the left side of Table I. The flavor wave model only requires the 6 parameters listed on the right side of Table I to reproduce the experimentally observed gap and magnetic field dependence. We note that the magnetic field dependence is reproduced by our two models up to fields of 22 T. The details of the models are presented in Ref. [35]. In the latter, we also show how it reproduces the magnetic field [26], the temperature dependence of the magnetization, and the magnon dispersions [13,14].

This ring-exchange term is not accessible within the expansion of the Hamiltonian bilinear in the $\tilde{S} = 1/2$ operators considered in Refs. [13,14] which, because of its emergent $U(1)$ symmetry, only has gapless excitations at the zone center. We also note that we found the flavor wave model considered in Ref. [14] to be gapless even when including spin-orbital interactions. This is why we must go beyond these previous models to explain the opening of the gap. In Ref. [35], we discuss other symmetry allowed terms in the flavor wave model that can open a gap. These terms, however, are not allowed within the $\tilde{S} = 1/2$ model, which is equivalent to the flavor wave model when only the lowest two energy levels are taken into account, and thus we do not consider them as possible explanations for the gap opening.

In Ref. [14], the finite magnon gap at the zone center was proposed to open by a quantum order-by-disorder mechanism [34]. The magnon dispersion was assumed to obey the phenomenological formula $\tilde{\omega}(\mathbf{k}) = \sqrt{\Delta^2 + \omega(\mathbf{k})^2}$, with Δ being the zone center magnon gap induced by quantum fluctuations. In contrast, by including the ring-exchange terms, we can obtain the magnon dispersion within our two models without any *ad hoc* assumptions. Our theoretical results agree with data from neutron scattering (see Ref. [35] for the calculated magnon dispersion), Raman spectroscopy (with magnetic field), and TDTS. Therefore, we conclude that the ring-exchange interaction is the origin of the gap at the zone center in $CoTiO_3$.

The ring-exchange interaction also explains the selection rules associated with the absorption due to magnons in Fig. 2. We write the normal modes of the four zone-center magnons, when the equilibrium spins point in the $\pm x$ direction, in the following form: $\tilde{S}[(\tilde{S}^y_{1,1}, \tilde{S}^z_{1,1}), (\tilde{S}^y_{1,2}, \tilde{S}^z_{1,2}), (\tilde{S}^y_{2,1}, \tilde{S}^z_{2,1}), (\tilde{S}^y_{2,2}, \tilde{S}^z_{2,2})]$, where $\tilde{S}^{\beta}_{\mu,\nu}$ is the oscillating part of the spin along the β axis, in

TABLE I. Models for magnon gap opening and magnetic field dependence. The effective $\tilde{S} = 1/2$ model uses the same bilinear exchange interaction values as in Ref. [14], while the flavor wave model is a modified version of the model in Ref. [14], both with external magnetic field $\boldsymbol{B}$. In the effective $\tilde{S} = 1/2$ model, $\tilde{H}_{\rm bl}$ is the Hamiltonian that is bilinear on the effective $\tilde{S} = 1/2$ operators with up to sixth nearest-neighbor exchange interactions ($\tilde{J}_1$, $\tilde{J}_3$, and $\tilde{J}_5$ in plane and $\tilde{J}_2$, $\tilde{J}_4$, and $\tilde{J}_6$ out of plane) of the XXZ type, as shown in Fig. 1(a), for $\tilde{S} = 1/2$ spins. $\tilde{H}_6$ is the ring-exchange interaction with strength $\tilde{\alpha}_6$; here $\tilde{\phi}_6$ represents a phase that determines the direction of the magnetic moment in the honeycomb plane and it equals π. $\tilde{H}_{\rm Z}$ is the Zeeman energy of interaction between the magnetic moments and and in-plane magnetic field with an effective g factor, $\tilde{g}_{\parallel}$. In the flavor wave model, H_0 is the single Co^{2+} ion Hamiltonian where λ is the atomic spin-orbit energy, δ is the oxygen octahedron trigonal distortion energy, $S = 3/2$, and effective $l = 1$. $H_{\rm bl}$ is the bilinear spin interactions and contains only isotropic (Heisenberg) nearest-neighbor exchange (J_1 in plane and J_4 out of plane). H_6 is the ring-exchange interaction with strength α_6 and phase $\phi_6 = \pi$. $H_{\rm Z}$ is the corresponding Zeeman energy. Uncertainties are estimated from fitting the Raman data and the neutron scattering data from Ref. [14].

Effective $\tilde{S} = 1/2$ model	Flavor wave model
$\tilde{H} = \tilde{H}_{\rm bl} + \tilde{H}_6 + \tilde{H}_{\rm Z}$	$H = H_0 + H_{\rm bl} + H_6 + H_{\rm bq} + H_{\rm Z}$
	$H_0 = \sum_{\boldsymbol{r},i}(3\lambda/2)\boldsymbol{S}_{\boldsymbol{r},i}\cdot\boldsymbol{l}_{\boldsymbol{r},i} + \delta[(l^z_{\boldsymbol{r},i})^2 - 2/3]$
$\tilde{H}_{\rm bl} = \frac{1}{2}\sum_{\boldsymbol{r},\delta\boldsymbol{r}}\sum_{i,j}\tilde{\boldsymbol{S}}^{\mathsf{T}}_{\boldsymbol{r},i}\tilde{\boldsymbol{J}}^{ij}_{\delta\boldsymbol{r}}\tilde{\boldsymbol{S}}_{\boldsymbol{r}+\delta\boldsymbol{r},j}$	$H_{\rm bl} = \frac{1}{2}\sum_{\boldsymbol{r},\delta\boldsymbol{r}}\sum_{i,j}\boldsymbol{S}^{\mathsf{T}}_{\boldsymbol{r},i}\boldsymbol{J}^{ij}_{\delta\boldsymbol{r}}\boldsymbol{S}_{\boldsymbol{r}+\delta\boldsymbol{r},j}$
$\tilde{H}_6 = \tilde{\alpha}_6\left(e^{-i\tilde{\phi}_6}\sum_{\boldsymbol{r}}\prod_{i=1}^{6}\tilde{S}^{+}_{\boldsymbol{r}+\delta^{\rm ring}_i} + \text{H.c.}\right)$	$H_6 = \alpha_6\left(e^{-i\phi_6}\sum_{\boldsymbol{r}}\prod_{i=1}^{6}S^{+}_{\boldsymbol{r}+\delta^{\rm ring}_i} + \text{H.c.}\right)$
	$H_{\rm bq} = \frac{1}{2}\sum_{\langle ri,r'j\rangle}[q(S^{+}_{ri})^2(S^{-}_{r'j})^2 + q^*(S^{-}_{ri})^2(S^{+}_{r'j})^2]$
$\tilde{H}_{\rm Z} = \mu_{\rm B}\sum_{\boldsymbol{r},i}\tilde{g}_{\parallel}(B^x\tilde{S}^x_{\boldsymbol{r},i} + B^y\tilde{S}^y_{\boldsymbol{r},i})$	$H_{\rm Z} = \mu_{\rm B}\sum_{\boldsymbol{r},i}\boldsymbol{B}\cdot(2\boldsymbol{S}_{\boldsymbol{r},i} - 3\boldsymbol{I}_{\boldsymbol{r},i}/2)$
$\tilde{J}^{xx}_1 = \tilde{J}^{yy}_1 = -6.36$ meV, $\tilde{J}^{zz}_1 = 1.97$ meV	J_1=−0.90(2) meV
$\tilde{J}^{xx}_2 = \tilde{J}^{yy}_2 = -0.33$ meV, $\tilde{J}^{zz}_2 = 0.30$ meV	
$\tilde{J}^{xx}_3 = \tilde{J}^{yy}_3 = 0.78$ meV, $\tilde{J}^{zz}_3 = 0.15$ meV	
$\tilde{J}^{xx}_4 = \tilde{J}^{yy}_4 = 0.11$ meV, $\tilde{J}^{zz}_4 = 0.32$ meV	$J_4 = 0.189(8)$ meV
$\tilde{J}^{xx}_5 = \tilde{J}^{yy}_5 = -0.39$ meV, $\tilde{J}^{zz}_5 = 0.20$ meV	
$\tilde{J}^{xx}_6 = \tilde{J}^{yy}_6 = 0.79$ meV, $\tilde{J}^{zz}_6 = 0.68$ meV	
$\tilde{g}_{\parallel} = 2.73(3)$	
	$\delta = 52(2)$ meV
	$\lambda = 16.4(2)$ meV
$\tilde{\alpha}_6 = 46(6)$ μeV	$\alpha_6 = 0.62(7)$ μeV
	$q = -0.15(1)$ meV

layer μ and sublattice ν. Without the ring exchange, the lowest-energy mode would be gapless, i.e., a Goldstone mode due to $U(1)$ symmetry in the XXZ model. Its normal mode, within the $\tilde{S} = 1/2$ approximation, is $\tilde{S}[(0.5, 0), (0.5, 0), (-0.5, 0), (-0.5, 0)]$. This means that the spins only deviate from the equilibrium direction in the hexagonal plane and have no net magnetic moment associated with it because $\sum_{\mu,\nu}\tilde{S}^{\beta}_{\mu,\nu} = 0$ for both $\beta = y$ and $\beta = z$. However, with the ring-exchange interaction, the normal mode becomes $\tilde{S}[(0.5, 0.03\text{i}), (0.5, 0.03\text{i}), (-0.5, 0.03\text{i}), (-0.5, 0.03\text{i})]$ as shown in Fig. 4(b). Thus, this magnon has a net magnetic dipole moment along the c axis ($\sum_{\mu,\nu}\tilde{S}^{z}_{\mu,\nu} \neq 0$), consistent with the TDTS data shown in Fig. 2(b), where the absorption due to this pseudo-Goldstone mode happens only when $\boldsymbol{h}_{\omega} \parallel c$ axis.

The normal mode for the 5.4-meV magnon does not qualitatively change with the addition of the ring exchange and keeps its net magnetic moment in the honeycomb plane. Thus, it can be excited by $\boldsymbol{h}_{\omega} \parallel$ to the honeycomb plane, i.e., $\sum_{\mu,\nu}\tilde{S}^{y}_{\mu,\nu} \neq 0$ as shown in Figs. 2(a) and 2(c). Its normal mode, shown in Fig. 4(c), is $\tilde{S}[(0.45, 0.23\text{i}), (0.45, 0.23\text{i}), (0.45, -0.23\text{i}), (0.45, -0.23\text{i})]$. This mode is the one whose energy decreases toward 0 around 17 T as shown in Fig. 3(b). Its intensity vanishes in the fully polarized state as a result of the magnon being at the Brillouin zone's edge along the k_z direction, which is thus Raman inactive. We can tell this is the case because its normal mode has y-axis spin oscillations of opposite sign for the two layers along the c axis, making its periodicity (two layers) twice the unit cell (one layer) in the fully polarized state. The details of the normal modes of the other two zone-center magnons are given in Ref. [35].

Finally, we address the topic of topologically protected surface magnons in $CoTiO_3$ by analyzing the symmetry indicators [17,18,21] of the magnon wave functions within the $\tilde{S} = 1/2$ model. The symmetry indicators of the bond-centered inversion symmetry ($\mathcal{I}$) of the two lower magnon modes imply that, when there is a gap between them in the entire Brillouin zone, both magnon bands must have odd Chern numbers. The magnetic inversion symmetry $\tilde{\mathcal{I}}$ (defined in Ref. [35]), however, forces the Chern number to vanish when magnons are energetically separated from each other. Because the Chern number cannot be both an odd integer and 0 simultaneously, these magnon bands must cross somewhere in the Brillouin zone. Experiments show that they intersect at two nodal lines around the hexagonal Brillouin zone's corners (K and K′ points) [13,14] and are reproduced here with our modeling [35]. These nodal lines are topologically

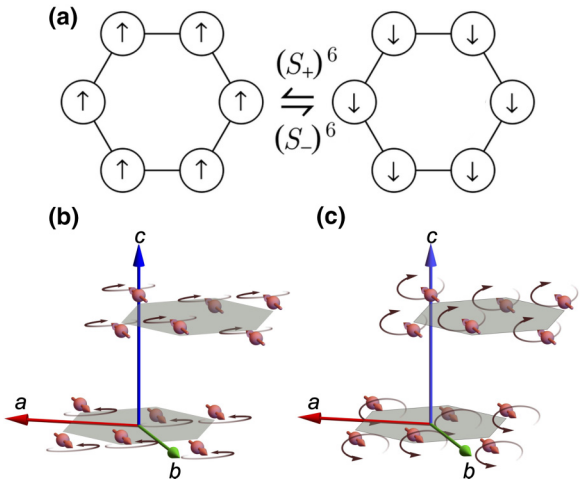

FIG. 4. Ring-exchange interaction and magnon normal modes. (a) Ring-exchange interaction considered in both the $\tilde{S} = 1/2$ and the flavor wave models. Normal modes for the pseudo-Goldstone mode and the 5.4-meV mode are shown in panels (b) and (c), respectively, where only two honeycomb layers are shown. The faded black arrows are the oscillations of the magnetic moments.

protected by the magnetic inversion $\tilde{\mathcal{I}}$ and are characterized by a nontrivial first Stiefel-Whitney number [42]. However, this symmetry is generally broken by an open surface, and thus $CoTiO_3$ cannot have protected topological magnons on its surfaces.

IV. CONCLUSIONS

In summary, with the combination of TDTS, magneto-Raman spectroscopy, and theoretical modeling we determined that the origin of the magnon gap in $CoTiO_3$ is a ring-exchange interaction between the magnetic moments in the honeycomb plane. We found that this interaction acts the same way in both the flavor wave model and the effective $\tilde{S} = 1/2$ approximation. By applying a magnetic field along the honeycomb plane, we determined the field dependence of the two lowest magnon energies. This allowed us to refine the values of the exchange interactions in the Hamiltonians used to model the experiment. A surprisingly small value for the ring-exchange interaction is responsible for the ≈ 0.9-meV magnon gap. The ring-exchange interaction also explains the selection rules for magnon absorption in the TDTS experiment. It is an exciting possibility that the ring-exchange interaction plays a significant role in the physics of other quantum magnets. Furthermore, we showed that no protected topological magnons can occur on the surface of $CoTiO_3$. More generally, this work demonstrates the power of combining TDTS, magneto-Raman spectroscopy, and theoretical modeling to study magnon excitations in quantum magnets.

ACKNOWLEDGMENTS

Work at OSU and CSU was supported by the Center for Emergent Materials at OSU, a Materials Research Science and Engineering Center funded by the NSF under Grant No. DMR-2011876. A.J.B. and A.R.H.W. acknowledge the NIST Innovation in Measurement Science (IMS) program for funding.

Y.L., E.V.J., D.M.H., C.L., and A.G. built the TDTS system and obtained and analyzed the TDTS data at OSU. T.T.M., J.R.S., T.A., and M.F.M. obtained and analyzed the Raman data at NIST. A.P. and C.F. obtained the Raman data at LNCMI. Y.L., M.K., J.G., Y.M.L., N.T., and K.F.G. performed theoretical analysis and calculations to explain the magnon spectrum and its magnetic field dependence. T.D.L., D.S., and K.R. grew, cut, and oriented the single crystals of $CoTiO_3$ used in this work. A.J.B. and R.L.D. performed magnetization measurements and additional Laue x-ray diffraction on the single crystals. R.V.A. and Y.L. wrote the manuscript with input from all the coauthors. R.V.A. generated the initial idea for this project. A.R.H.W., N.T., Y.M.L., and R.V.A. supervised all the work.

The authors declare that they do not have any competing financial interests.

The identification of any commercial product or trade name does not imply endorsement or recommendation by the National Institute of Standards and Technology.

[1] W. Heisenberg, Mehrkörperproblem und resonanz in der quantenmechanik, Z. Phys. **38**, 411 (1926).

[2] W. Heisenberg, Zur theorie des ferromagnetismus, Z. Phys. **49**, 619 (1928).

[3] P. Dirac, Quantum mechanics of many-electron systems, Proc. R. Soc. A **123**, 714 (1929).

[4] R. B. Kummer, E. D. Adams, W. P. Kirk, A. S. Greenberg, R. M. Mueller, C. V. Britton, and D. M. Lee, Effects of a magnetic field on nuclear spin ordering in solid ^{3}He, Phys. Rev. Lett. **34**, 517 (1975).

[5] H. Godfrin, G. Frossati, A. S. Greenberg, B. Hébral, and D. Thoulouze, Observation of solid ^{3}He ordering at melting pressures in high magnetic fields, Phys. Rev. Lett. **44**, 1695 (1980).

[6] D. D. Osheroff, M. C. Cross, and D. S. Fisher, Nuclear antiferromagnetic resonance in solid ^{3}He, Phys. Rev. Lett. **44**, 792 (1980).

[7] M. Roger, J. H. Hetherington, and J. M. Delrieu, Magnetism in solid ^{3}He, Rev. Mod. Phys. **55**, 1 (1983).

[8] M. Roger, Ring exchange and correlated fermions, J. Phys. Chem. Solids **66**, 1412 (2005).

[9] S. Sugai, M. Sato, T. Kobayashi, J. Akimitsu, T. Ito, H. Takagi, S. Uchida, S. Hosoya, T. Kajitani, and T. Fukuda, High-energy spin excitations in the insulating phases of high-T_c superconducting cuprates and La_2NiO_4, Phys. Rev. B **42**, 1045 (1990).

[10] R. Coldea, S. M. Hayden, G. Aeppli, T. G. Perring, C. D. Frost, T. E. Mason, S.-W. Cheong, and Z. Fisk, Spin waves and electronic interactions in La_2CuO_4, Phys. Rev. Lett. **86**, 5377 (2001).

[11] W. G. F. Krüger, W. Chen, X. Jin, Y. Li, and L. Janssen, Triple-q order in $Na_2Co_2TeO_6$ from proximity to hidden-SU(2)-symmetric point, Phys. Rev. Lett. **131**, 146702 (2023).

[12] C. Lee, Y. Sun, L. Ye, S. Rathi, K. Wang, Y.-M. Lu, J. Moore, J. Checkelsky, and J. Orenstein, Spin wavepackets in the kagome ferromagnet Fe_3Sn_2: Propagation and precursors, Proc. Natl. Acad. Sci. USA **120**, e2220589120 (2023).

[13] B. Yuan, I. Khait, G.-J. Shu, F. C. Chou, M. B. Stone, J. P. Clancy, A. Paramekanti, and Y.-J. Kim, Dirac magnons in a honeycomb lattice quantum *XY* magnet $CoTiO_3$, Phys. Rev. X **10**, 011062 (2020).

[14] M. Elliot, P. A. McClarty, D. Prabhakaran, R. D. Johnson, H. C. Walker, P. Manuel, and R. Coldea, Order-by-disorder from bond-dependent exchange and intensity signature of nodal quasiparticles in a honeycomb cobaltate, Nat. Commun. **12**, 3936 (2021).

[15] M. Z. Hasan and C. L. Kane, Colloquium: Topological insulators, Rev. Mod. Phys. **82**, 3045 (2010).

[16] N. P. Armitage, E. J. Mele, and A. Vishwanath, Weyl and Dirac semimetals in three-dimensional solids, Rev. Mod. Phys. **90**, 015001 (2018).

[17] H. C. Po, A. Vishwanath, and H. Watanabe, Symmetry-based indicators of band topology in the 230 space groups, Nat. Commun. **8**, 50 (2017).

[18] B. Bradlyn, L. Elcoro, J. Cano, M. G. Vergniory, Z. Wang, C. Felser, M. I. Aroyo, and B. A. Bernevig, Topological quantum chemistry, Nature (London) **547**, 298 (2017).

[19] P. A. McClarty, Topological magnons: A review, Annu. Rev. Condens. Matter Phys. **13**, 171 (2022).

[20] F. Lu and Y.-M. Lu, Magnon band topology in spin-orbital coupled magnets: Classification and application to α-$RuCl_3$, arXiv:1807.05232.

[21] M. J. Karaki, X. Yang, A. J. Williams, M. Nawwar, V. Doan-Nguyen, J. E. Goldberger, and Y.-M. Lu, An efficient material search for room temperature topological magnons, Sci. Adv. **9**, eade7731 (2023).

[22] Y. Ishikawa and S.-I. Akimoto, Magnetic property and crystal chemistry of ilmenite ($MeTiO_3$) and hematite (α-Fe_2O_3) system I. Crystal chemistry, J. Phys. Soc. Jpn. **13**, 1110 (1958).

[23] Y. Ishikawa and S.-I. Akimoto, Magnetic property and crystal chemistry of ilmenite ($MeTiO_3$) and hematite (α-Fe_2O_3) system II. Magnetic property, J. Phys. Soc. Jpn. **13**, 1298 (1958).

[24] S. Klemme, W. Hermes, M. Eul, C. H. Wijbrans, A. Rohrbach, and R. Pöttgen, New thermodynamic data for $CoTiO_3$, $NiTiO_3$, and $CoCO_3$ based on low-temperature calorimetric measurements, Chem. Cent. J. **5**, 54 (2011).

[25] A. M. Balbashov, A. A. Mukhin, V. Y. Ivanov, L. D. Iskhakova, and M. E. Voronchikhina, Electric and magnetic properties of titanium-cobalt-oxide single crystals produced by floating zone melting with light heating, Low Temp. Phys. **43**, 965 (2017).

[26] M. Hoffmann, K. Dey, J. Werner, R. Bag, J. Kaiser, H. Wadepohl, Y. Skourski, M. Abdel-Hafiez, S. Singh, and R. Klingeler, Magnetic phase diagram, magnetoelastic coupling, and Grüneisen scaling in $CoTiO_3$, Phys. Rev. B **104**, 014429 (2021).

[27] R. E. Newnham, J. H. Fang, and R. P. Santoro, Crystal structure and magnetic properties of $CoTiO_3$, Acta Crystallogr. **17**, 240 (1964).

[28] A. Abragam and B. Bleaney, *Electron Paramagnetic Resonance of Transition Ions* (Oxford University Press, Oxford, 1970).

[29] R. Sano, Y. Kato, and Y. Motome, Kitaev-Heisenberg Hamiltonian for high-spin d^7 Mott insulators, Phys. Rev. B **97**, 014408 (2018).

[30] H. Liu and G. Khaliullin, Pseudospin exchange interactions in d^7 cobalt compounds: Possible realization of the Kitaev model, Phys. Rev. B **97**, 014407 (2018).

[31] H. Liu, J. Chaloupka, and G. Khaliullin, Kitaev spin liquid in 3*d* transition metal compounds, Phys. Rev. Lett. **125**, 047201 (2020).

[32] A. Kitaev, Anyons in an exactly solved model and beyond, Ann. Phys. **321**, 2 (2006).

[33] B. Yuan, M. B. Stone, G.-J. Shu, F. C. Chou, X. Rao, J. P. Clancy, and Y.-J. Kim, Spin-orbit exciton in a honeycomb lattice magnet $CoTiO_3$: Revealing a link between magnetism in *d*- and *f*-electron systems, Phys. Rev. B **102**, 134404 (2020).

[34] J. G. Rau, P. A. McClarty, and R. Moessner, Pseudo-Goldstone gaps and order-by-quantum disorder in frustrated magnets, Phys. Rev. Lett. **121**, 237201 (2018).

[35] See Supplemental Material at http://link.aps.org/supplemental/10.1103/PhysRevB.109.184436 for a description of the crystal growth and characterization, spectroscopic experimental methods, and expanded details of the theoretical models. The Supplemental Material also contains Refs. [43–51].

[36] T. T. Mai, C. Svoboda, M. T. Warren, T.-H. Jang, J. Brangham, Y. H. Jeong, S.-W. Cheong, and R. Valdés Aguilar, Terahertz spin-orbital excitations in the paramagnetic state of multiferroic $Sr_2FeSi_2O_7$, Phys. Rev. B **94**, 224416 (2016).

[37] M. T. Warren, G. Pokharel, A. D. Christianson, D. Mandrus, and R. Valdés Aguilar, Terahertz dielectric analysis and spin-phonon coupling in multiferroic GeV_4S_8, Phys. Rev. B **96**, 054432 (2017).

[38] J. J. Stickler, S. Kern, A. Wold, and G. S. Heller, Magnetic resonance and susceptibility of several ilmenite powders, Phys. Rev. **164**, 765 (1967).

[39] T. T. Mai *et al.* (unpublished).

[40] R. A. Muniz, Y. Kato, and C. D. Batista, Generalized spin-wave theory: Application to the bilinear-biquadratic model, Prog. Theor. Exp. Phys. **2014**, 83I01 (2014).

[41] S. Das, S. Voleti, T. Saha-Dasgupta, and A. Paramekanti, Xy magnetism, Kitaev exchange, and long-range frustration in the $J_{\rm eff} = \frac{1}{2}$ honeycomb cobaltates, Phys. Rev. B **104**, 134425 (2021).

[42] J. Ahn, S. Park, D. Kim, Y. Kim, and B.-J. Yang, Stiefel-Whitney classes and topological phases in band theory, Chin. Phys. B **28**, 117101 (2019).

[43] T. Seifert, S. Jaiswal, U. Martens, J. Hannegan, L. Braun, P. Maldonado, F. Freimuth, A. Kronenberg, J. Henrizi, I. Radu, E. Beaurepaire, Y. Mokrousov, P. M. Oppeneer, M. Jourdan, G. Jakob, D. Turchinovich, L. M. Hayden, M. Wolf, M. Münzenberg, M. Kläui *et al.*, Efficient metallic spintronic emitters of ultrabroadband terahertz radiation, Nat. Photonics **10**, 483 (2016).

[44] K. Liu, J. Xu, and X.-C. Zhang, GaSe crystals for broadband terahertz wave detection, in *Nonlinear Optics: Materials, Fundamentals and Applications* (Optica, Hawaii, USA, 2004), p. MC7.

[45] E. V. Jasper, T. T. Mai, M. T. Warren, R. K. Smith, D. M. Heligman, E. McCormick, Y. S. Ou, M. Sheffield, and R. Valdés Aguilar, Broadband circular polarization time-domain terahertz spectroscopy, Phys. Rev. Mater. **4**, 013803 (2020).

[46] A. McCreary, T. T. Mai, F. G. Utermohlen, J. R. Simpson, K. F. Garrity, X. Feng, D. Shcherbakov, Y. Zhu, J. Hu, D. Weber, K. Watanabe, T. Taniguchi, J. E. Goldberger, Z. Mao, C. N.

Lau, Y. Lu, N. Trivedi, R. Valdés Aguilar, and A. R. Hight Walker, Distinct magneto-Raman signatures of spin-flip phase transitions in CrI_3, Nat. Commun. **11**, 3879 (2020).

[47] A. McCreary, J. R. Simpson, T. T. Mai, R. D. McMichael, J. E. Douglas, N. Butch, C. Dennis, R. Valdés Aguilar, and A. R. Hight Walker, Quasi-two-dimensional magnon identification in antiferromagnetic $FePS_3$ via magneto-Raman spectroscopy, Phys. Rev. B **101**, 064416 (2020).

[48] D. G. Smillie, J. C. Pickering, G. Nave, and P. L. Smith, The spectrum and term analysis of Co III measured using Fourier transform and grating spectroscopy, Astrophys. J. **223**, 11 (2016).

[49] G. W. Pratt and R. Coelho, Optical absorption of CoO and MnO above and below the Néel temperature, Phys. Rev. **116**, 281 (1959).

[50] J. Colpa, Diagonalization of the quadratic boson Hamiltonian, Phys. A (Amsterdam, Neth.) **93**, 327 (1978).

[51] S. Toth and B. Lake, Linear spin wave theory for single-$\boldsymbol{Q}$ incommensurate magnetic structures, J. Phys.: Condens. Matter **27**, 166002 (2015).